CrossMark

Mapping of potential lunar landing areas using LRO and SELENE data

A.A. Kokhanov [a],[*], I.P. Karachevtseva [a], A.E. Zubarev [a], V. Patraty [a], Zh.F. Rodionova [b], J. Oberst [c],[d]

[a] MIIGAiK Extraterrestrial Laboratory (MExLab), Moscow State University of Geodesy and Cartography (MIIGAiK), Moscow, Russia
[b] Sternberg State Astronomical Institute Lomonosov Moscow University, Moscow, Russia
[c] Technical University of Berlin, Berlin, Germany
[d] German Aerospace Center (DLR), Berlin, Germany

ABSTRACT

We apply cartographic methods on remote sensing data obtained by Lunar Reconnaissance Orbiter (LRO) and Kaguya (SELENE) to characterize potential landing sites for the "Luna-25" mission, previously selected. To identify presumable hazards (steep slopes, high ruggedness, cratered terrain) we developed special algorithms and GIS-tools. Sets of hazard maps for 3 high-priority potential landing sites were created.

1. Introduction

Beginning with the mission of «Luna-1» in 1959, the Moon enjoyed an extensive early exploration by orbiters and landers. However, while the early lunar landings were limited to the mid-latitudes, nowadays, it is the lunar subpolar areas (±65°–85° latitudes), which are in the focus of lunar science.

In 1996, observations of reflected radio signals from "Clementine" hinted at the abundance of hydrogen within southern polar area (Nozette et al., 1996). Remote sensing data from Lunar Prospector, which operated from lunar polar orbit during 1998–1999, have shown a high probability for the abundance of hydrogen near the poles (Binder, 1998). The abundance of hydrogen was confirmed by the LCROSS impact experiment (Colaprete et al., 2010). Later, the area distribution of neutron flux was mapped by the Lunar Exploration Neutron Detector (LEND) (Sanin et al., 2012) onboard the Lunar Reconnaissance Orbiter (LRO). Bounds of areas with a low neutron flux were refined, indicative for the abundance of hydrogen. Significant deposits are confined to the Polar Regions and especially to permanently shadowed areas (PSAs) (Sanin, 2015). According to DIVINER measurements, temperatures can fall below 20 K within PSAs

(Sefton-Nash et al., 2013), which may represent cold traps for volatiles and the most probable places of water ice concentration (McClanahan et al., 2015). Also albedo measurements of permanently shadowed regions by LAMP show that they are darker at far-UV wavelengths (Gladstone et al., 2012), presumably indicating about 2% water frost there. According to Mini-RF data, there is a water ice cover of 661.53 km^2 near the South Pole (Calla et al., 2015).

With the great interest in possible water repositories on the moon, ROSCOSMOS plans to launch several spacecraft to the southern subpolar area of the Moon (Efanov and Dolgopolov, 2016), never studied by landed spacecraft before.

2. "Luna-25" mission and south subpolar areas of interest

"Luna-25" is planned for launch and landing in a lunar subpolar area in 2019, later to be followed by the Orbiter "Luna-26" and the lander "Luna-27". The aim of the "Luna" missions is to study polar resources and the lunar exosphere, and in particular, to confirm the abundance of polar water ice, thus to begin a long-term exploration of the Moon (Khartov, 2015). For "Luna-25" 12 potential landing sites (PLS) were selected by the Space Research Institute of Russian
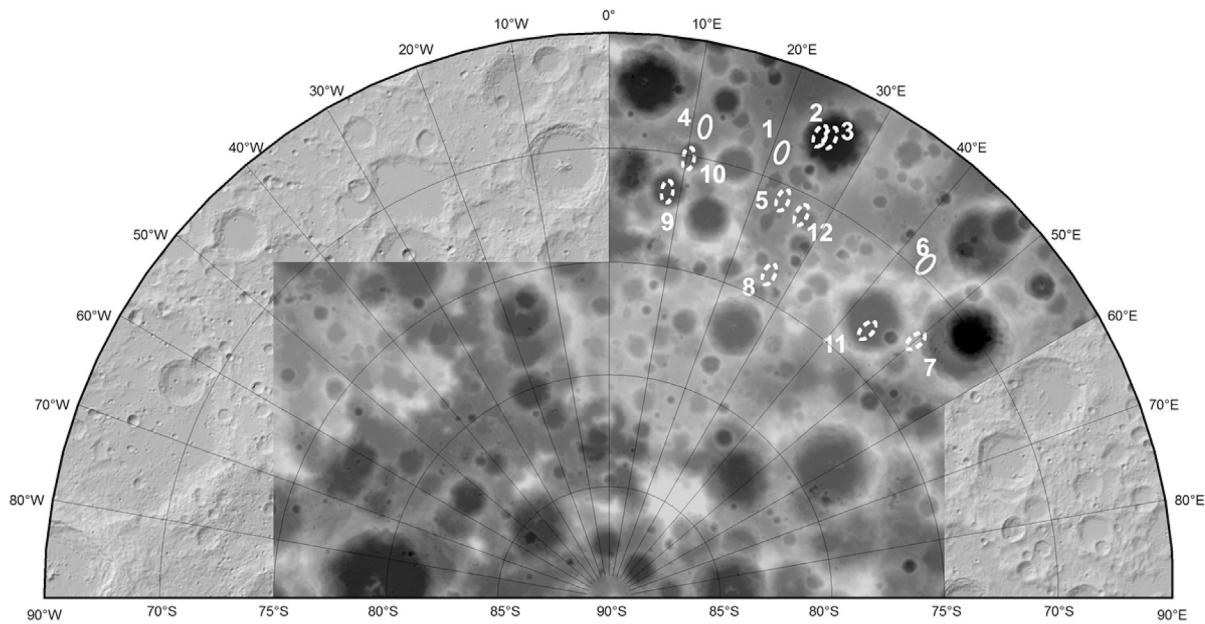
Fig. 1. Coverage of ROI by LRO data. Background – hillshaded GLD100 (Scholten et al., 2012). Tiles of LDEM 1024, covers PLS are shown. Ellipses – PLS of "Luna-25". The three PLS 1, 4, and 6 with the highest priority, studied in this paper, are shown by solid line.

Table 1
Coordinates of PLS with the highest priority.

N°[a]	Latitude	Longitude
1	**−68.77**	**21.21**
2	−67.48	24.61
3	−67.37	25.70
4	**−68.65**	**11.55**
5	−70.68	23.63
6	**−69.54**	**43.54**
7	−72.16	50.08
8	−73.88	26.36
9	−71.71	08.18
10	−70.15	10.29
11	−73.40	44.00
12	−70.93	26.71

[a] PLS coordinates and numbering are given according to Mitrofanov et al. (2016). Priority sites (studied in this paper) are marked in bold.

Academy of Science (Mitrofanov et al., 2016, Fig. 1) according to following criteria:

- Region of interest is limited by 65–85°S and 0–60°E;
- The landing ellipse must be 15 × 30 km (spread in North-South direction);
- Surface slopes at the landing site must be less than 7° at a baseline of 2.5 m;
- The illumination level within the landing area must be more 40% over the day;
- The Earth position above horizon should be more than 10°;
- Significant resources of Water Equivalent Hydrogen (more than 0.2%), which is calculated as the ratio of neutron count value in the studied area to reference (mid-latitude) value (Sanin et al., 2016).

Three of 12 PLSs – 1, 4, 6 – have the highest priority (Fig. 1). In this paper, we focus on the three highest-priority landing sites based on study of their morphometric parameters (Table 1). Base spatial data for selection in research (Mitrofanov et al., 2016) were LDEM 1 024 (see paragraph 3) and LEND Data.

Taking into account these criteria we calculated various morphometric characteristics of the surface, surrounding selected ellipses: slopes, roughness, depth (relative depth) of craters. Additionally, we created illumination and visibility maps.

3. LRO and Kaguya data

Although remote sensing data and derived products cover most part of the Lunar surface, high-resolution topographic data are rarely available for the PLSs. For comprehensive characterization of PLSs we use the entire array of LRO data and supplement it by Kaguya data for local relief study (Table 2, Fig. 1).

3.1. LRO NAC images

The high-resolution images obtained by the LRO Narrow Angle Camera (NAC) (Robinson et al., 2010) are very much suited for studies of
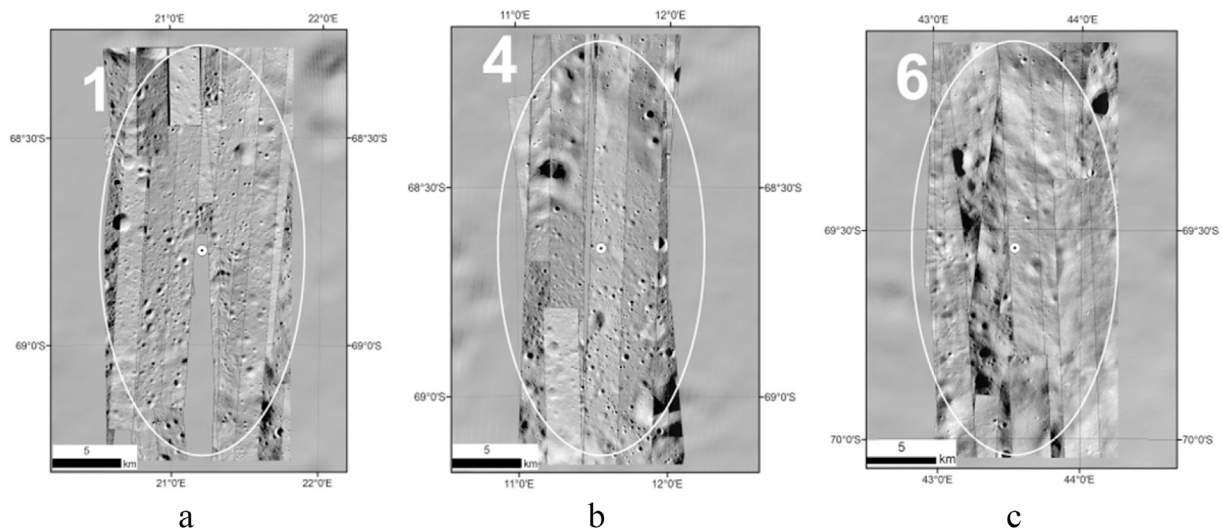
Table 2
Remote sensing data available for the subpolar areas.

Product	Type	Spatial resolution, m/pixel	Source
LRO NAC	Orthoimages	0.5–1.3	Robinson et al., 2010
TC Ortho map	Orthomosaic	7	Haruyama et al., 2008
Kaguya SLDEM 2013	DEM	7	Haruyama et al., 2014
LDEM 1024	DEM	30	Neumann et al., 2011

Fig. 2. Coverage of the landing ellipses 1 (a), 4 (b), 6 (c) by LRO NAC images.
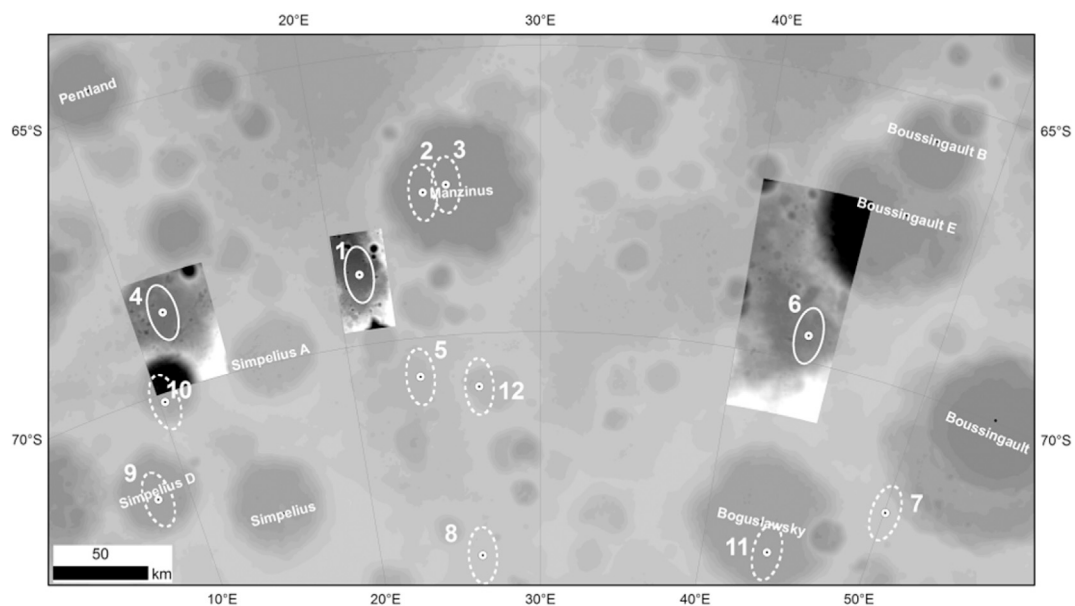

Fig. 3. Coverage of the three high-priority sites by SLDEM2013. Background: GLD100.

potential landing sites. On average one NAC panchromatic image covers a surface area of 30 km × 2.5 km with resolution up to 0.5 m. The EDR (Experimental Data Record) images were orthorectified and co-registered for mapping in GIS. The LRO NAC images provide information on the distribution of craters and slopes over small baselines, using the technique of shadowed-area analysis (Abdrakhimov et al., 2015).

To cover the PLS we selected about 80 single NAC images (Appendix A), but with gaps remaining (Fig. 2). The landing ellipse 6 has the most complete coverage (Fig. 2c). More recently, LRO images were specifically taken to cover ellipse 4. The camera was tilted to produce stereo viewing. PLSs were processed for high-resolution DEM generation for this ellipse (see chapter 4.3 for details).

3.2. LOLA coverage

Topographic profiles from LOLA (Neumann et al., 2011) cover subpolar regions of interest with nominal resolution of 30 m/pixel. As the individual raw (irregularly spaced) laser altimeter tracks are difficult to use in a statistical characteristics of area topography, we use the LDEM_1 024 (Lunar Orbiter Laser Altimeter Digital Elevation Model), which is provided as gridded raster data (Neumann et al., 2011), projected in simple cylindrical projection with nominal resolution 1 024 pixel/deg (30 m/pixel).

3.3. Kaguya images

The TC (Terrain Camera) on Selene obtained stereo images with near-global coverage. Kaguya DEMs, obtained by photogrammetric processing (Haruyama et al., 2014), are available in grid format. The SLDEM2013 tiles cover areas of 1° × 1° (Fig. 3) and have resolutions of 10 m (approximately equal to the source TC images). However, according to estimates by Barker et al. (2016) the effective resolution of the model is ~100 m. Also, vertical quantization is rather coarse (1 m), and internal
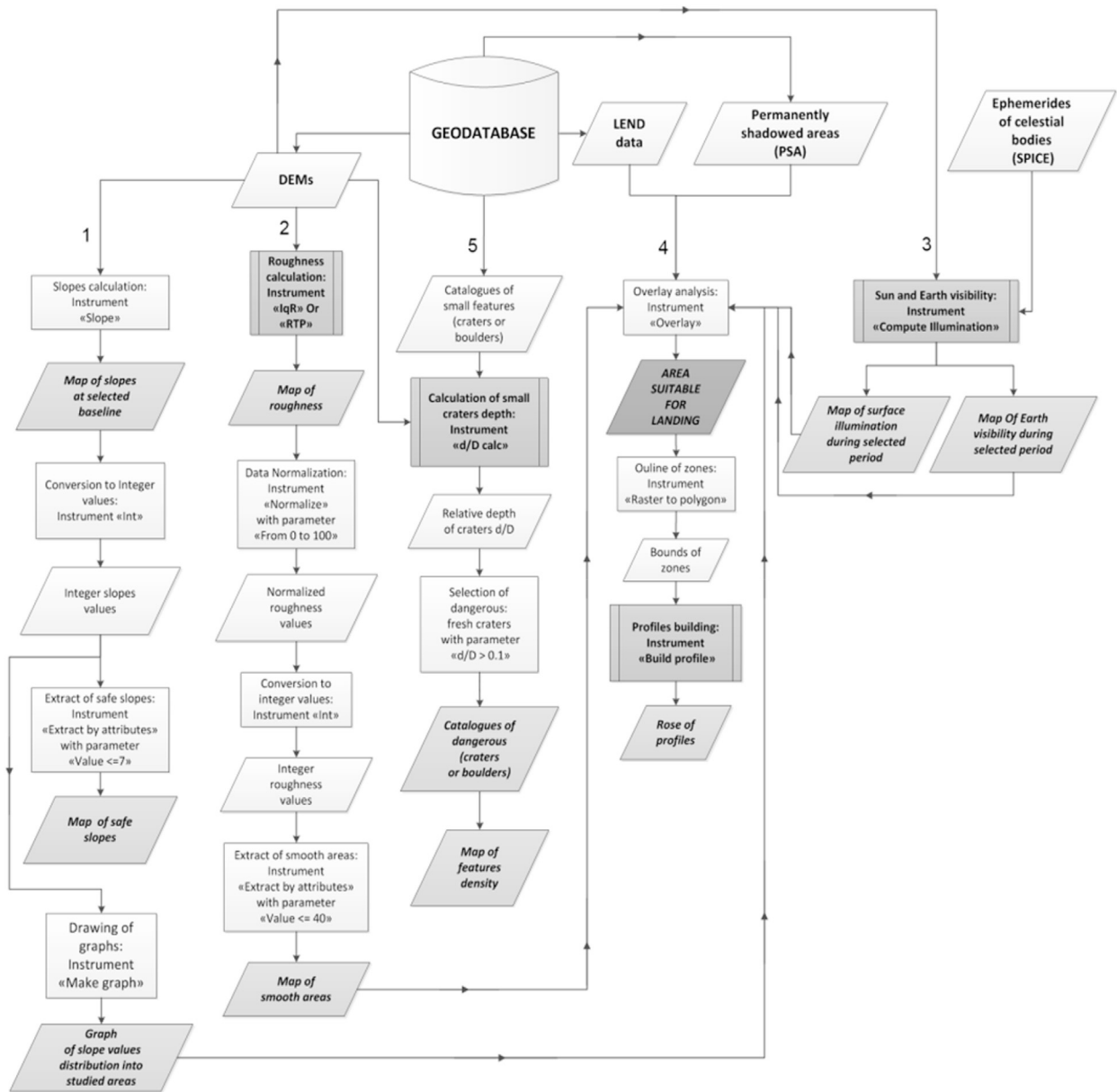
Fig. 4. Automated GIS-algorithm for landing site characterization, including tools (bold) and results of intermediate calculations (italic).
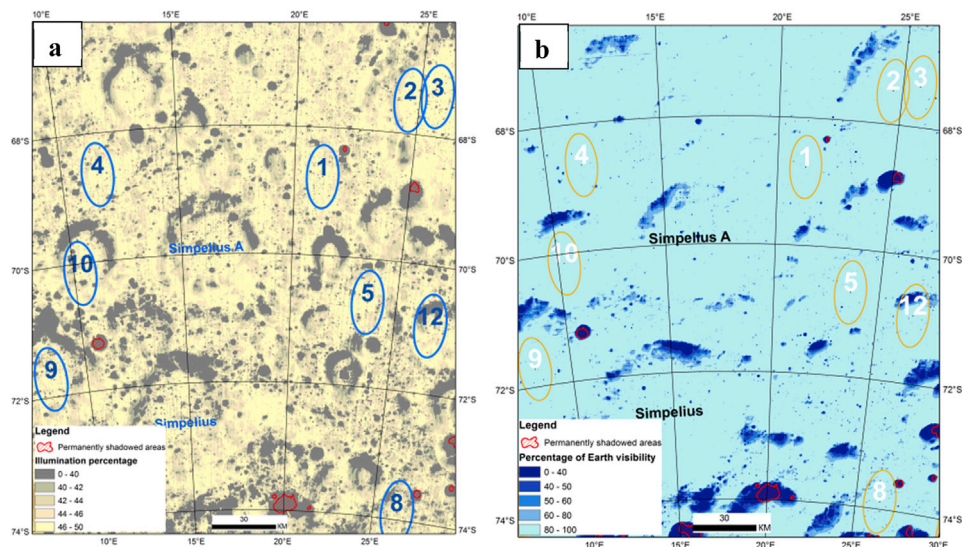

Fig. 5. Maps of illumination (a) and Earth visibility (b) during period 03.11.2019–30.01.2020 for area of PLS based on LDEM1024.

Table 3
Parameters of LROC NAC stereo pairs used for DEM production.

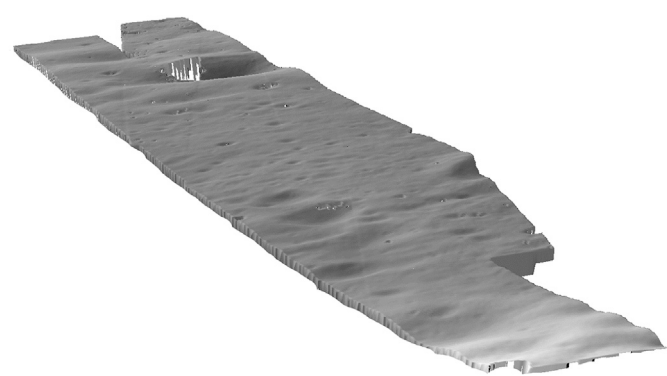| Number of pairs	Image IDs	Angle of convergence,°	Nominal elevation accuracy, m
1	1144692407_1225998203	16.1	1.4
2	1149401504_1225998203	15.6	1.6
3	1149401504_1225998204	12.6	2
4	1195391099_1225998204	14.6	1.7
5	1197746696_1225998203	17.1	1.5
6	1225998203_1195391099	14.6	1.3
7	1225998203_159873359	15.5	1.6
8	1225998203_183437918	18.9	1.3
9	1225998204_1197746694	12.1	1.9
10	124503307_1225998204	12.9	0.9
11	183437918_1225998204	16.5	1.5

Fig. 6. Digital elevation model for the part of landing ellipse 4. Vertical scale is magnified by a factor 2.

vertical precision is limited (~10 m). Still, this dataset covers all ellipses and has highest spatial resolution among the available DEMs. We use these data to calculate relief parameters of the PLS at detailed level in the neighborhood of landing ellipses.

4. Methods

The local level of mapping considers direct hazards for the landing of spacecraft at baselines equal to the spacecraft footprint or close to it in case of lack of sufficient resolution data. Using high-resolution DEMS and specially developed GIS-tools we can detect and measure small craters (size more 100 m and less 1 km), calculate short baseline morphometric characteristics of surface and consider the influence of relief on the visibility of Earth and Sun.

4.1. GIS-tools

For safe landing it is necessary to conduct a comprehensive study of the surface characteristics for the candidate sites. Using scientific and engineering criteria proposed for safety of landing sites (Mitrofanov et al., 2016) we have developed algorithms to obtain data, which describe small-scale surface characteristics on the basis of topographic data (Fig. 4):
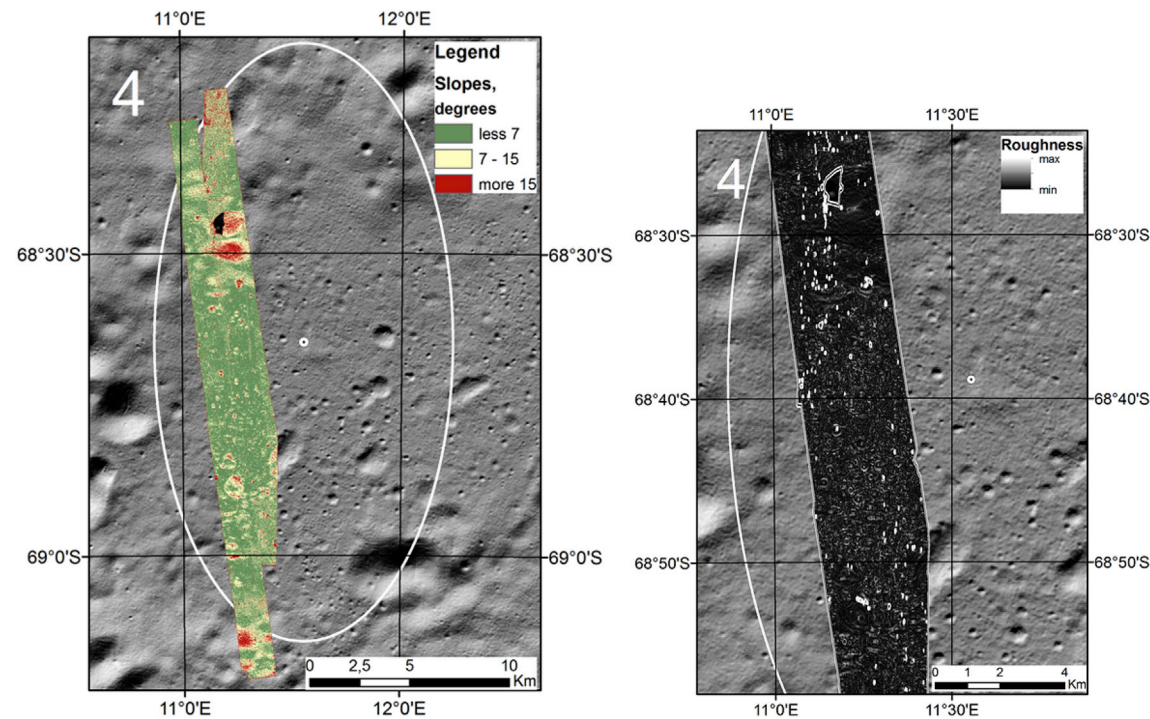

Fig. 7. Map of short-scale slopes on baseline 4 m (left) and roughness (right) for parts of landing ellipse 4. Background: hillshaded SLDEM2013.
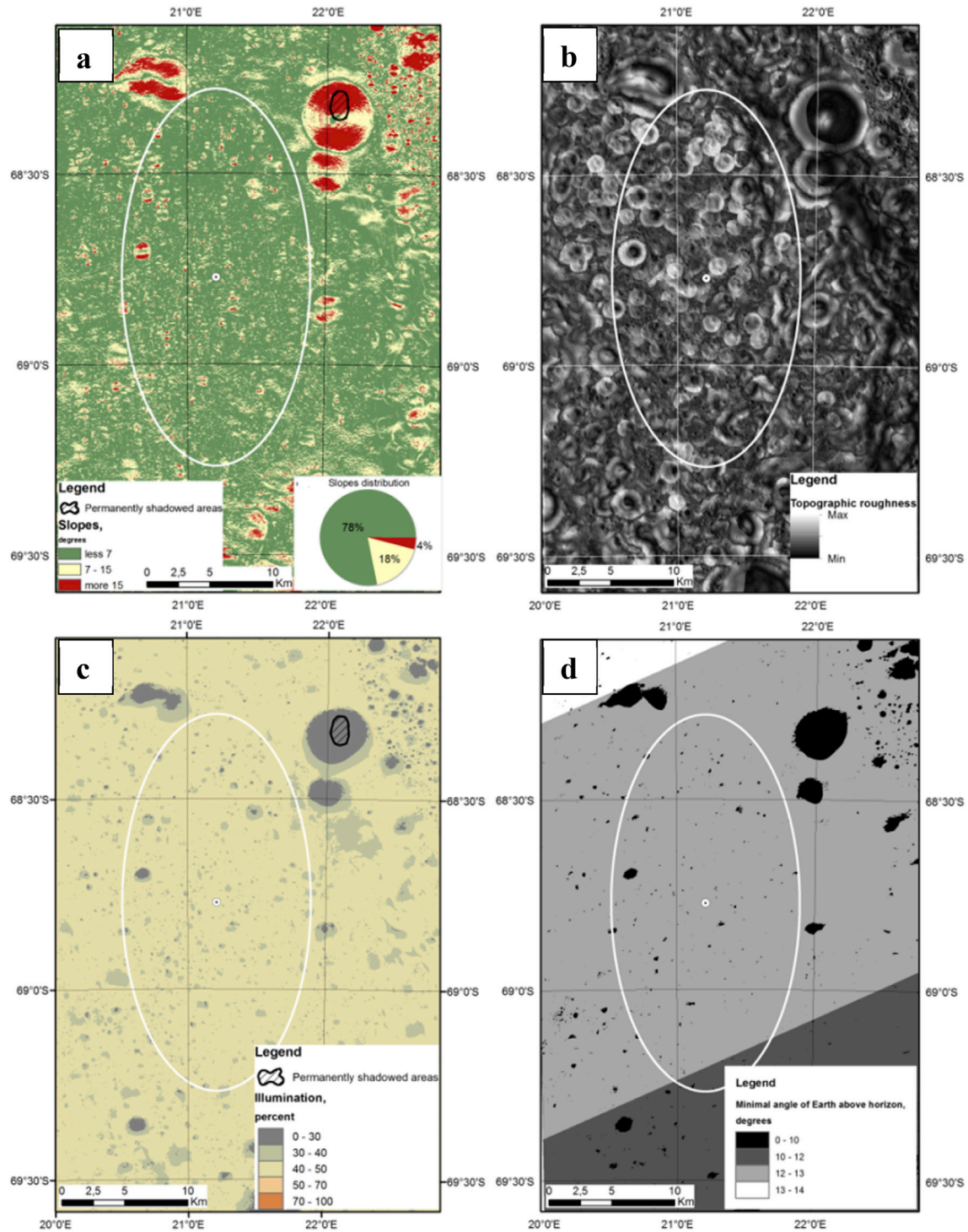
Fig. 8. Maps of hazards for the landing ellipse 1: a) slopes on baseline 20 m; b) topographic roughness as relative topographic position; c) percentage of illumination during period 03.11.2019–30.01.2020; d) minimal angle of Earth above horizon during period 03.11.2019–30.01.2020.
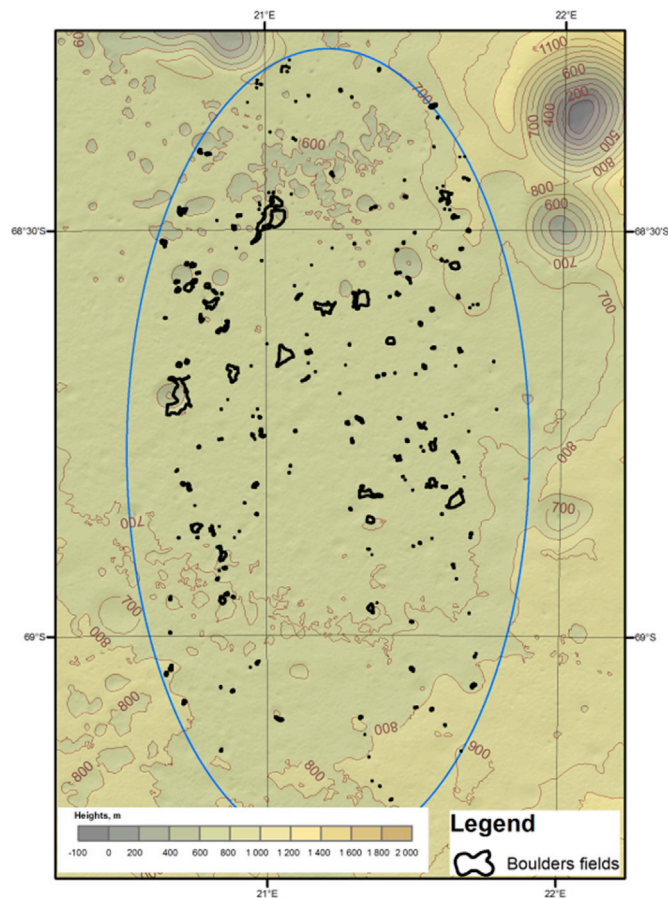
Fig. 9. Hypsometric map with distribution of boulder fields inside the first ellipse.
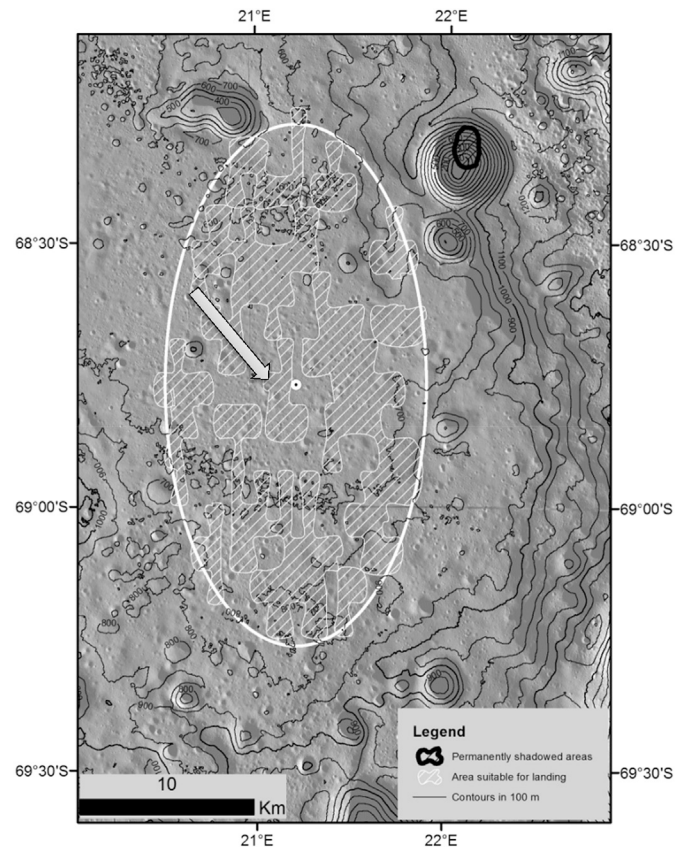

Fig. 10. Topographic map of the landing ellipse 1 with results of overlay analysis. Background: Kaguya images TCO_MAP_02_S66E018S69E021SC, TCO_MAP_02_S66E021-S69E024SC, TCO_MAP_02_S69E018S72E021SC, TCO_MAP_02_S69E018S72E021SC. The selected for further detailed analysis area is marked by arrow.

- Slopes on baseline 15 m were calculated using the Horn method (Horn, 1981). The 1st step of developed algorithm (Fig. 4) creates digital raster models of slope distribution and diagram of slopes less 7°.
- Roughness was calculated from Kaguya SLDEM 2013 by relative topographic position method (RTP, Tagil and Jenness, 2008): this parameter was calculated within moving circular windows with radius of 80 m as ratio of differences: "mean height – minimal height" to "maximal height – minimal height". With this method, we obtain digital raster models which separate cratered and smooth areas and which highlight crater edges, local peaks and pits. It was calculated with instrument «RTP» (2nd step of algorithm).

To demonstrate Sun and Earth visibility we created additional maps (step 3 on Fig. 4) using the DEM and given ephemeris data (SPK, https://naif.jpl.nasa.gov/pub/naif/toolkit_docs/C/req/spk.html). We use local horizon modeling as demonstrated by Zubarev et al. (2016). Analysis of ROI using LDEM 1 024 shows that Sun and Earth visibility are limited on south-oriented slopes of craters (Fig. 5). 84% of the area is illuminated by 40% and more during the period 03.11.2019–30.01.2020.

At the next stage (4 on Fig. 4) we searched for areas, which combined safe slopes, smooth terrain, good illumination, and which were of scientific interest (in this case, areas associated with a low neutron flux). Through the geometrical center of such areas, roses of profiles were drawn. As a result of such analysis we obtain maps, showing areas free of potential hazards.

Selected areas were characterized by topographic profiles and by maps of crater distribution and density. From DEMs with sufficient resolution the degradation stages of craters can evaluated. Fresh craters may be identified, which could pose a hazard for landing. We define "fresh" craters as those with relative depth (Depth/Diameter) of more than 0.15. The depths of craters are calculated using the 5th step of developed algorithm (5 on Fig. 4).

As results of application of the algorithm we obtained special maps for the three high-priority landing ellipses, which characterize the relief of the studied surface, topographic profiles and safe areas within PLS.

4.2. LRO NAC DEM production

To identify steep slopes at short (<10 m) baselines of the lander footprint, we have created a high-resolution DEM for parts of landing ellipse 4 using photogrammetric techniques (Karachevtseva et al., 2017; Zubarev et al., 2016). The production of the DEM is based on bundle block adjustment of coordinate measurements by least squares analysis techniques using overlapping stereo images. We used 11 LROC NAC stereo-pairs (Table 3, Appendix A). Within all images 91 tie-points were collected; the average number of measurements for each tie-point, using various images, is 3.5 and the maximum is 6. The coordinate accuracy on the lunar surface were estimated as $RMS_x = \pm0.3$ m, $RMS_y = \pm1.0$ m, $RMS_z = \pm3.5$ m. Subsequently, dense image matching was carried out to produce a DEM with a ground pixel size of 2 m. The DEM has a vertical resolution 10 m (Fig. 6).

The DEM covers an area 79.6 km^2 and allows to calculate slopes at baselines of ~4 m. The nominal accuracy of elevation is 1.7 m. The minimal height at the covered area is 490 m in the unnamed crater
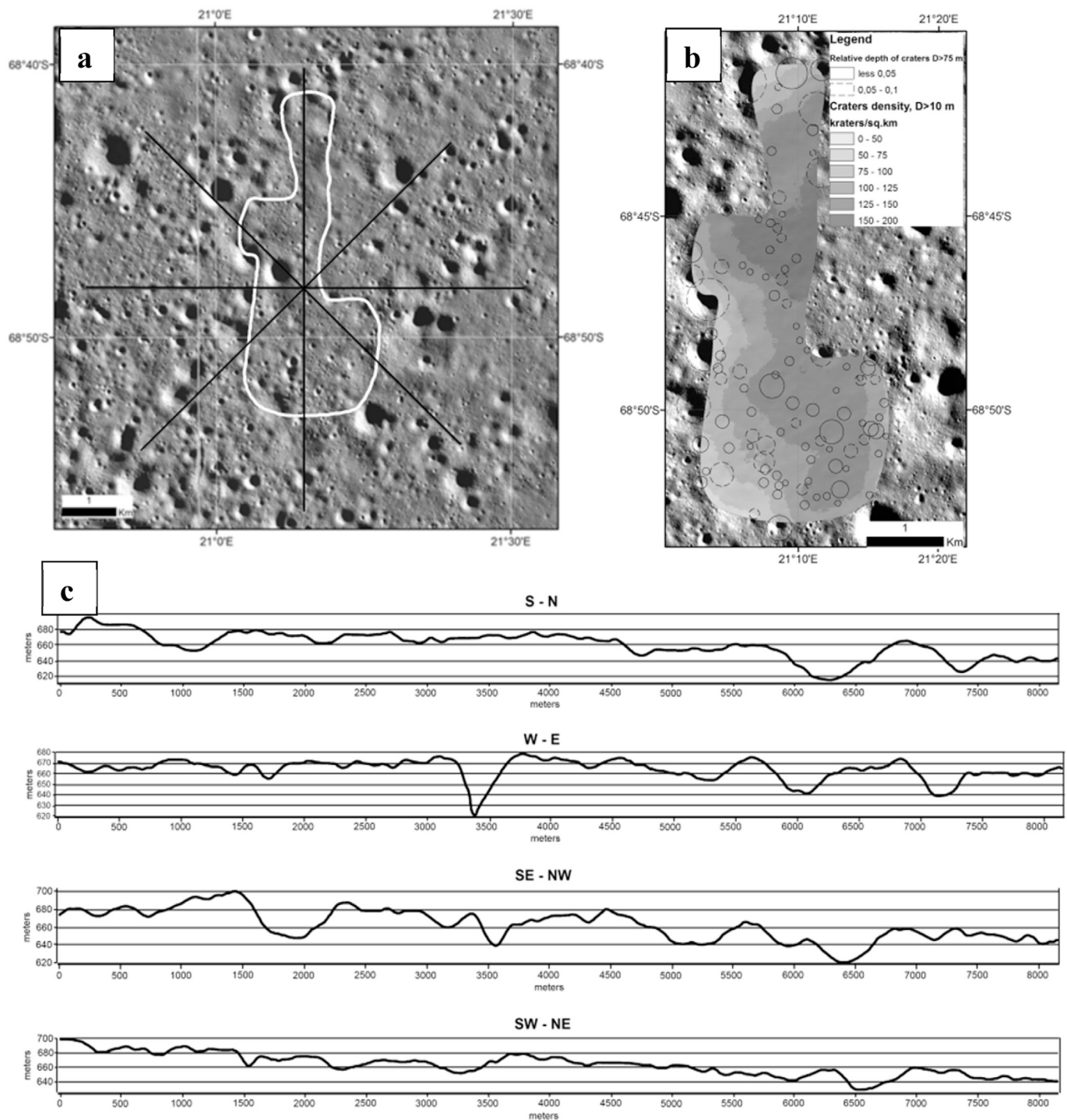
Fig. 11. Detailed characteristics for the central area of the landing ellipse 1: a) topographic profiles directions; b) map of small craters (D > 10 m) density; c) topographic profiles across the area.

bottom, the maximal – 1 225 m on the south, the rim of crater Simpelius E. The mean height of the area is 720 m. The surface is relatively flat and has a general slope to the south-south-east direction and then again rises towards the craters rim. Slopes less than 7° cover 67% of the studied area, slopes between 7° and 15° occur within 27% of the area (Fig. 7). Also a map of roughness was compiled (Fig. 7).

5. Results

Using Kaguya data we have characterized potential landing sites

(PLS) at highest available spatial resolution (10 m/pixel against 30 m/pixel by LDEM at −68° latitude). Maps of hazards (Fig. 8) identify critical rugged areas for landing of a spacecraft, characterized by steep slopes of more than 7°, low illumination of less than 40%, low angle of Earth above the horizon of less than 10°. PLSs are represented as ellipses elongated along meridian with big axis 30 km and small axis 15 km.

For the first landing ellipse, fields of boulders were outlined, which pose a particular hazard for landing. Unfortunately, the coverage by NAC images excludes the central lower part of the ellipse. Typically, boulder
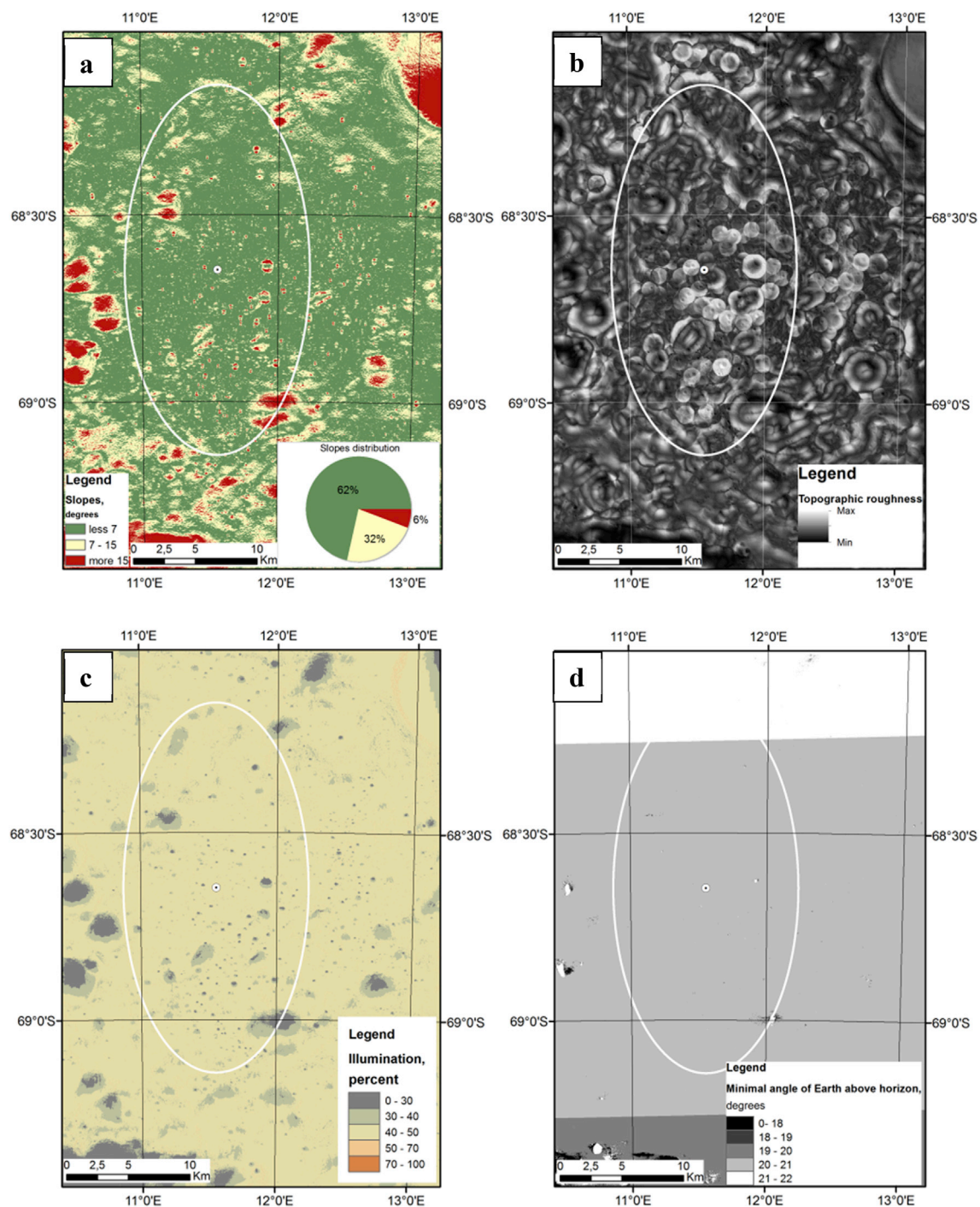
Fig. 12. Maps of hazards for the landing ellipse 4: a) slopes on baseline 20 m; b) topographic roughness as relative topographic position; c) percentage of illumination during period 03.11.2019–30.01.2020; d) minimal angle of Earth above horizon during period 03.11.2019–30.01.2020.

fields are confined to the bottoms of large fresh craters or nearby areas beyond the crater rims. But several boulders are found far from such craters. Fig. 9 shows rough outlines of boulder fields.

The analysis shows that 78% of the landing ellipse 1 are safe in terms of the slope criterion; 93% of the area are illuminated more than 40% during the period of 03.11.2019–30.01.2020. There is concern about topographic depressions, where the local horizon for the observer hides the Sun and Earth during most part of the observation period. 51% of territory are suitable by all criteria (Fig. 10). As the studied area is situated higher than 65°S, to consider permanently shadowed areas in GIS

we used gridded spatial data (Mazarico et al., 2011, http://ode.rsl.wustl.edu/moon/indexproductsearch.aspx).

The central area of the ellipse was characterized in more detail. Intersecting topographic profiles were created along (S—N) and across approach trajectory of spacecraft as additional reference information. Inspection of our crater catalog reveals that there are no fresh craters larger than 70 m in diameter in this area. Also a map of density of small craters was created to account for those small craters which escape automatic depth measurements from the DEM (Fig. 11).
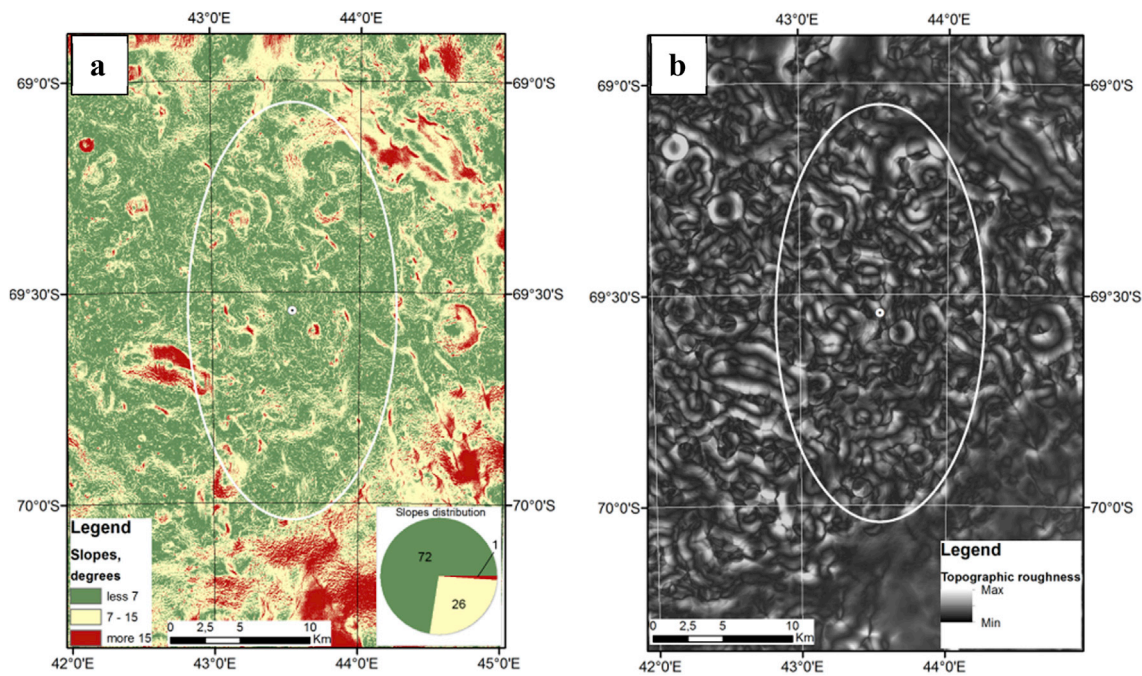
Fig. 13. Maps of hazards for the landing ellipse 6: a) slopes on baseline 20 m; b) topographic roughness as relative topographic position.

The landing ellipse 4 (Fig. 12) has a limited fraction of areas with safe values of slopes (62%). Also, there are several hazardous craters inside the area. 91% of the landing ellipse are illuminated by more than 40% of the foreseen mission period. Landing ellipse 6 (Fig. 13) has large areas with safe slopes similar to landing ellipse 1, but the ellipse is surrounded by hazardous short-baseline slopes.

6. Conclusions

The work was aimed at a comprehensive study of the Moon's subpolar areas and proposed spacecraft landing sites. For three landing ellipses with high-priority we created maps of hazards, including slopes, roughness, illumination, and Earth visibility. We used the common overlay method for presenting morphometric parameters and outlining of zones with low level of hazards and high scientific priority. We developed tools to automatize most of the morphometric GIS-analysis and estimation of Sun- and Earth-visibility for landing site analysis. In future studies DIVINER data will be added to overlay analysis to improve estimation of hydrogen abundance inside studied areas.

Small craters appear to be the main hazards for landing. Hence, we have created crater catalogues for several parts of ROI and tools for morphometric characterization. As there is a great number of small craters inside each of PLSs, it is impossible to detect each crater manually within limited time (Ivanov et al., 2016). In this work we used spatial and statistical analysis at local scale as indirect methods to find areas nearly free of craters.

Southern subpolar area is characterized by low-elevation sun, making it difficult to obtain a DEM from available LRO NAC images for the studied ROIs by photogrammetric methods. For accurate and reliable prognosis of dangerous factors on baselines at the scale of landing-modules we have created a DEM for parts of landing ellipse 4. Morphometric calculation shows, that most parts of the area are occupied by slopes less than 7°. To carry out further analysis on short baselines for the entire landing area we look forward to additional high-resolution LRO data for this area.

Appendix A. List of NAC images covering the three high-priority landing ellipses

	Image ID	Resolution, m	Solar azimuth, °	Incidence angle, °	Image ID	Resolution, m	Solar azimuth, °	Incidence angle, °	Image ID	Resolution, m	Solar azimuth, °	Incidence angle, °
	landing ellipse 1				landing ellipse 4				landing ellipse 6			
1	M1096373957	0.93	162.28	83.22	M1096438231	0.89	161.23	82.52	M106592075	0.53	121.65	71.8
2	M1098731891	0.92	135.75	74.5	M1108226620	0.88	203.19	80.31	M1111491759	0.74	165.47	83.61
3	M1103446893	0.49	261.07	67.45	M1111711925	0.87	162.14	83.07	M1118559229	0.71	260.53	70.67
4	M1114006000	0.77	134.7	75.11	M1127080034	0.89	163.69	83.55	M1120917015	0.67	230.14	76.56
5	M111444639	0.6	241.22	70.4	M1134154641	0.48	260.12	68.44	M1123269187	0.74	205.14	83.28
6	M1116357174	0.75	106.99	70.78	M113868663	1.06	214.39	77.22	M113665144	0.6	216.44	75.99
7	M1116364281	0.76	106.94	70.51	M1144692407[a]	0.83	137.09	74.96	M1138661979	1.03	206.07	79.2
8	M1138804162	0.88	204.59	79.73	M1149401504[a]	0.87	256.45	70.44	M1142111318	0.69	167.43	84.08
9	M1144621309	0.72	137.88	75.25	M1154106887	1.07	202.75	82.64	M1153886196	0.93	204.48	83.18
10	M1146974905	0.45	106.98	70.5	M1157708115	1.05	162.98	84.43	M1172716033	0.87	167.24	83.87

(*continued*)

	Image ID	Resolution, m	Solar azimuth, °	Incidence angle, °	Image ID	Resolution, m	Solar azimuth, °	Incidence angle, °	Image ID	Resolution, m	Solar azimuth, °	Incidence angle, °
	landing ellipse 1				landing ellipse 4				landing ellipse 6			
11	M1164712025	0.54	260.69	67.67	M1184709197	0.99	201.72	83.72	M1188124163	0.83	163.21	85.31
12	M1169424813	1.04	204.2	79.31	M1195391099[a]	0.44	257.89	68.13	M1190478543	0.83	138.3	75.89
13	M1172879492	0.89	164.84	83.53	M1197746694[a]	0.66	230.97	71.93	M1203317483	0.51	165.63	83.33
14	M1188257650	0.66	162.61	83.99	M124503307[a]	1.08	88.49	70.88	M124279285	0.94	93.14	70.16
15	M1190619093	0.66	135.62	75.32	M159873359	1.05	221.44	76.4	M126634774	0.91	243.41	73.68
16	M119719076	0.98	147.42	78.53	M165776285	1.01	158.11	81.16	M137273299	1.2	129.16	72.67
17	M126797627	0.96	240.91	71.33	M183437918[a]	0.91	131.26	74.09	M144349709	1.19	222.23	74.23
18	M137408970	1.13	128.04	70.9	M188148550	0.9	253.92	70.51	M152572366	0.9	127.63	74.78
19	M150380885	0.94	153.67	80.71	M192866400	0.88	199.35	83.67	M157288254	0.87	250.02	72.03
20	M155096843	0.95	98.12	69.97	M1225998203[a]	0.46	265.01	68.29	M157295044	0.86	252.18	71.65
21	M159805504	0.94	220.45	76.45	M1225998204[a]				M165579544	1.19	159.73	82.96
22	M162167015	0.93	194.95	84.42					M167934397	1.09	132.98	74.78
23	M181014726	0.83	158.83	81.99					M167941185	1.1	133.01	74.43
24	M183373589	0.82	131.88	74.81					M175011522	0.96	227.3	72.55
25	M190443132	0.79	226.72	76.11					M180857460	0.78	161.5	82.52
26	M192794923	0.77	200.2	83.76					M183216299	0.76	132.54	76.09
27									M185575174	0.75	105.19	72.45
28									M187926965	0.76	256.98	71.04

[a] New images used for high resolution DEM production.

References

Abdrakhimov, A.M., Basilevsky, A.T., Ivanov, M.A., Kokhanov, A.A., Karachevtseva, I.P., Head, J.W., 2015. Occurrence probability of slopes on the lunar surface: estimate by the shaded area percentage in the LROC NAC images. Sol. Syst. Res. 49 (5), 285–294. http://dx.doi.org/10.1134/S0038094615050019.

Barker, M.K., Mazarico, E., Neumann, G.A., Zuber, M.T., Haruyama, J., Smith, D.E., 2016. A new lunar digital elevation model from the Lunar Orbiter Laser Altimeter and SELENE Terrain Camera. Icarus 273, 346–355. http://dx.doi.org/10.1016/j.icarus.2015.07.039.

Binder, A.B., 1998. Lunar prospector: overview. Science 281 (4), 1475–1476.

Calla, O.P.N., Mathur, S., Gadri, K.L., Jangid, M., 2015. Quantification of water ice using Mini-SAR datasets over lunar poles. In: 46th Lunar and Planetary Science Conference. Abs. 1322.

Colaprete, A., Schultz, P., Heldmann, J., Wooden, D., Shirley, M., Ennico, K., Hermalyn, B., Marshall, W., Ricco, A., Elphic, R.C., Goldstein, D., Dummy, D., Bart, G.D., Asphaug, E., Korycancky, D., Landis, D., Sollitt, L., 2010. Detection of water in the LCROSS ejecta plume. Science 330 (60033). http://dx.doi.org/10.1126/science.1186986, 463–458.

Efanov V.V., Dolgopolov V.P. The Moon. 2016. From studies to exploration (on 50th anniversary of «LUNA-9» and «LUNA-10» satellites). Vestn. NPO Im. S.A. Lavochkina, 4, pp. 3–9 (in Russian).

Gladstone, G.R., Retherford, K.D., Egan, A.F., Kaufmann, D.E., Miles, P.F., Parker, J.W., Howarth, D., Rojas, P.M., Versteeg, M.H., Davis, M.W., Greathouse, T.K., Slater, D.C., Mukherjee, J., Steffl, A.J., Feldman, P.D., Hurley, D.M., Pryor, W.R., Hendrix, A.R., Mazarico, E., Stern, S.A., 2012. Far-ultraviolet reflectance properties of the Moon's permanently shadowed regions. J. Geophys. Res. 117, E00H04.

Haruyama, J., Matsunaga, T., Ohtake, M., Morota, T., Honda, C., Yokota, Y., Torii, M., Ogawa, Y., Lism Working Group, 2008. Global lunar-surface mapping experiment using the lunar imager/spectrometer on SELENE. Earth, Planets, Space 60, 243–255.

Haruyama, J., Ohtake, M., Matsunaga, T., Otake, H., Ishihara, Y., Masuda, K., Yokota, Y., Yamamoto, S., 2014. Data products of SELENE (Kaguya) terrain camera for future lunar missions. In: 45th Lunar and Planetary Science Conference, The Woodlands, 17–21 March, Abs. 1304.

Horn, B.K.P., 1981. Hill shading and the reflectance map. Proc. IEEE 69 (1), 14–47.

Ivanov, M.A., Abdrakhimov, A.M., Basilevsky, A.T., Demidov, N.E., Guseva, E.N., Head, J.W., Hiesinger, H., Krasilnikov, S.S., 2016. Geological characterization of the three most promising landing sites for the luna-glob mission. In: The 7th Moscow Solar System Symposium, 7MS3-MN-11.

Karachevtseva, I.P., Kozlova, N.A., Kokhanov, A.A., Zubarev, A.E., Nadezhdina, I.E., Patratiy, V.D., Konopikhin, A.A., Basilevsky, A.T., Abdrakhimov, A.M., Oberst, J., Haase, I., Jolliff, B.L., Plescia, J.B., Robinson, M.S., 2017. Cartography of the luna-21 landing site and lunokhod-2 traverse area based on lunar reconnaissance orbiter camera images and surface archive TV-panoramas. Icarus 283, 104–121.

Khartov, V.V., 2015. Ot issledovaniya k osvoeniyu resursov Luny. Vchera i zavtra (k 50-letiyu kosmicheskoi deyatel'nosti NPO imeni S.A. Lavochkina) (From research to the development of the resources of the Moon. Yesterday and tomorrow (to the 50th anniversary of Space activity of NPO Lavochkin)). Vestn. NPO Im. S. A. Lavochkina 3, 8–14.

Mazarico, E., Neumann, G.A., Smith, D.E., Zuber, M.T., Torrence, M.H., 2011. Illumination conditions of the lunar polar regions using LOLA topography. Icarus 211, 1066–1081.

McClanahan, T.P., Mitrofanov, I.G., Boynton, W.V., Chin, G., Bodnarik, J., Droege, G., Evans, L.G., Golovin, D., Hamara, D., Harshman, K., Litvak, M., Livengood, T.A., Malakhov, A., Mazarico, E., Milikh, G., Nandikotkur, G., Parsons, A., Sagdeev, R., Sanin, A., Starr, R.D., Su, J.J., Murray, J., 2015. Evidence for the sequestration of hydrogen-bearing volatiles towards the Moon's southern pole-facing slopes. Icarus 255, 88–99.

Mitrofanov, I., Djachkova, M., Litvak, M., Sanin, A., 2016. The method of landing sites selection for Russian lunar lander missions. Geophys. Res. Abstr. 18, EGU2016–10018.

Neumann, G.A., Smith, D.E., Scott, S., 2011. Lunar Reconnaissance Orbiter – Lunar Orbiter Laser Altimeter. ArchiveVolume – Software Interface Specification,. Version 2.5.

Nozette, S., et al., Nov. 1996. The Clementine bistatic radar experiment. Science 274 (5292), 1495–1498.

Robinson, M.S., Brylow, S.M., Tschimmel, M., Humm, D., Lawrence, S.J., Thomas, P.C., Denevi, B.W., Bowman-Cisneros, E., Zerr, J., Ravine, M.A., Caplinger, M.A., Ghaemi, F.T., Schaffner, J.A., Malin, M.C., Mahanti, P., Bartels, A., Anderson, J., Tran, T.N., Eliason, E.M., McEwen, A.S., Turtle, E., Jolliff, B.L., Hiesinger, H., 2010. The lunar reconnaissance orbiter camera (LROC) instrument overview. Space Sci. Rev. 150, 81–124.

Sanin, A.B., Mitrofanov, I.G., Litvak, M.L., Malakhov, A., Boynton, W.V., Chin, G., Droege, G., Evans, L.G., Garvin, J., Golovin, D.V., Harshman, K., McClanahan, T.P., Mokrousov, M.I., Mazarico, E., Milikh, G., Neumann, G., Sagdeev, R., Smith, D.E., Star, rR. D., Zuber, M.T., 2012. Testing lunar permanently shadowed regions for water ice: LEND results from LRO. J. Geophys. Res. 117, E00H26.

Sanin, A.B., 2015. Water maps of the polar Moon: LEND data after 6 years on the lunar orbit. In: 6th Solar System Symposium, 6MS3–MN10.

Sanin, A., Mitrofanov, I., Litvak, M., Boynton, W., Bodnarik, J., Hamara, D., Harshman, K., Chin, G., Evans, L., Livengood, T., McClanahan, T., Sagdeev, R., Srarr, R., 2016. How LEND sees the water on the Moon. Geophys. Res. Abstr. 18, EGU2016–7169.

Scholten, F., Oberst, J., Matz, K.-D., Roatsch, T., Wählisch, M., Speyerer, E.J., Robinson, M.S., 2012. GLD100: the near-global lunar 100 m raster DTM from LROC WAC stereo image data. J. Geophys. Res. 117, E00H17.

Sefton-Nash, E., Siegler, M.A., Paige, D.A., 2013. Thermal extremes in permanently shadowed regions at the lunar south pole. In: 44th Lunar and Planetary Science Conference, Houston. Abs. #2617.

Tagil, S., Jenness, J., 2008. GIS-based automated landform classification andtopographic, landcover and geologic attributes of landforms around the YazorenPolje. Turk. J. Appl. Sci. 8, 910–921.

Zubarev, A.E., Nadezhdina, I.E., Kozlova, N.A., Brusnikin, E.S., Karachevtseva, I.P., 2016. Special software for planetary image processing and research. The international archives of the photogrammetry. Remote Sens. Spatial Inf. Sci. 529–536. XLI-B4.

WEB-references

https://naif.jpl.nasa.gov/pub/naif/toolkit_docs/C/req/spk.html.
http://ode.rsl.wustl.edu/moon/indexproductsearch.aspx.